






Fermi surface and mass enhancement in the topological nodal-line semimetal NaAlSi

Shinya Uji ^{1,*}, Takako Konoike ¹, Yuya Hattori,¹ Taichi Terashima,¹ Tamio Oguchi ², Takahiro Yamada ³,
Daigorou Hirai ⁴ and Zenji Hiroi⁴

¹International Center for Materials Nanoarchitectonics, National Institute for Materials Science, Tsukuba, Ibaraki 305-0003, Japan

²Center for Spintronics Research Network, Osaka University, Toyonaka, Osaka 560-8531, Japan

³Institute of Multidisciplinary Research for Advanced Materials, Tohoku University, Sendai, Miyagi 980-8577, Japan

⁴Institute for Solid State Physics, University of Tokyo, Kashiwa, Chiba 277-8581, Japan



(Received 12 January 2022; revised 6 April 2022; accepted 12 May 2022; published 3 June 2022)

Quantum oscillations in the magnetic torque for the topological nodal-line semimetal NaAlSi with a superconducting transition at $T_c = 7$ K have been measured to investigate the Fermi surface. Four oscillation branches, α , β , γ , and δ are observed, whose frequency ranges from 40 to 380 T in magnetic fields parallel to the c axis. The results are consistent with the present first-principles band calculations, showing the presence of small Fermi surfaces elongated in the k_z direction. We obtain the large mass enhancement factors 2.0 for α and 3.1 for γ , ascribed to many-body effects likely responsible for the superconductivity. A nontrivial Berry phase is obtained for α , arising from the linear dispersion of the energy band.

DOI: [10.1103/PhysRevB.105.235103](https://doi.org/10.1103/PhysRevB.105.235103)

I. INTRODUCTION

New classes of nontrivial three-dimensional topological semimetals have inspired great interest because of intriguing electronic states with conic linear energy dispersions. In a Dirac semimetal, the band-crossing points, called Dirac points, are formed by fourfold-degenerated linear bands, where the quasiparticles are described as Dirac fermions. When time-reversal or space-inversion symmetry is broken in a Dirac semimetal, the fourfold-degenerated bands are split into two twofold ones, whose band-crossing points are called Weyl points. These Weyl semimetals have remarkable surface states, Fermi arcs, which are protected by the crystal symmetries.

In contrast to the Weyl or Dirac semimetals with the band crossing at a point, the nodal points extend along curves in the k space in so-called nodal-line semimetals. This nodal-line structure is recognized as a significant expansion of the nodal point, providing new opportunities to explore exotic topological nature. One of the most characteristic properties in the nodal-line semimetals is the formation of a surface state on the specified crystal surfaces, which are referred to as drumhead states. Superconductivity in these topological semimetals is of additional particular interest, which could lead to peculiar entanglement properties with the topological states [1–4].

The nodal-line semimetal NaAlSi has a tetragonal lattice with the space group $P4/nmm$ [5,6]. As shown in Fig. 1(a), each Al atom bonds with four Si atoms, forming a layer of two-dimensionally aligned Al-Si tetrahedra, that stacks with a Na bilayer along the c direction. First-principles calculations clarify that NaAlSi possesses nodal lines near the Fermi level E_F , which are protected from both the time-reversal and spatial-inversion symmetries [7–9]. Only small Fermi

surfaces are present although the details remain unclear [7,8]. Several drumhead states on the (001) surface are predicted [8,9], which have not been observed experimentally. NaAlSi is a type-II superconductor with a transition temperature $T_c \approx 7$ K at ambient pressure [10]. NaAlSi is isostructural to the “111” Fe-based superconductors LiFeAs ($T_c = 16$ -18 K) [11,12] and LiFeP ($T_c = 6$ K) [13], which are known as unconventional superconductors. In this way, NaAlSi provides us an excellent platform to search for unprecedented superconducting properties in nodal-line semimetals.

In hydrostatic pressure, T_c of NaAlSi increases up to ~ 8.35 K at 2 GPa and then the superconductivity vanishes at 4.8 GPa [14]. The muon spin rotation experiments [15] show that the superconductivity in NaAlSi has time-reversal symmetry and is fully gapped. The temperature dependence of the magnetic penetration length is well described by a two-gap model consisting of two s -wave symmetric gaps with $\Delta_1 = 0.6$ meV and $\Delta_2 = 1.39$ meV. In contrast, anisotropic superconducting gap behavior is suggested in the heat capacity data [6]. The Wilson ratio larger than unity, ~ 2.0 suggests strong electron correlation although the Fermi surfaces are formed by the wide s and p bands of Al and Si. These results suggest a certain unconventional aspect in the superconducting state. For further discussion on the superconductivity mechanism, the detailed structure of the Fermi surface is indispensable. In this study, we have performed magnetic torque measurements for single crystals of NaAlSi and observed quantum oscillations (QOs). We show that the Fermi surface structures obtained by the first-principles density-functional-theory (DFT) calculations well explain the QO measurements and the effective masses of the quasiparticles are significantly enhanced by many body effects.

II. METHODS

Single crystals of NaAlSi are synthesized by a Na flux method [6]. The chemical composition of the crystals

*uji.shinya@nims.go.jp

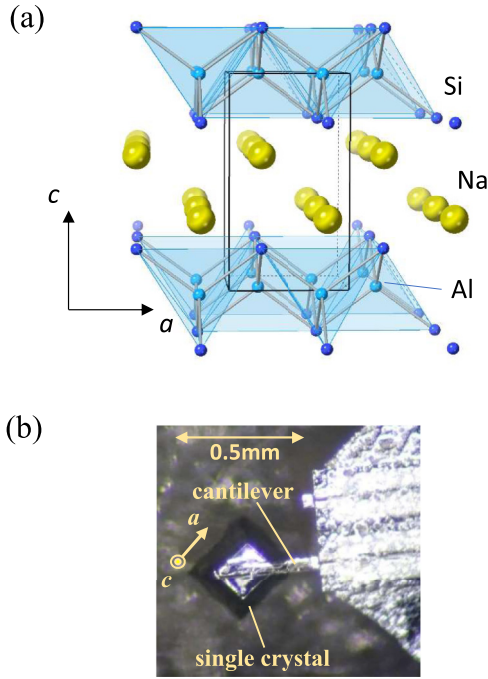


FIG. 1. (a) Crystal structure of NaAlSi. (b) Photo of microcantilever and single crystal of NaAlSi. The crystal is attached to the cantilever by silicon grease.

determined by a wavelength-dispersive x-ray spectrometer is in good agreement with the stoichiometric composition. The magnetic torque is measured by a piezoresistive microcantilever technique [16] as depicted in Fig. 1(b). As reported previously [6], the samples are unstable in the ambient atmosphere, probably due to reaction with moisture. The crystals immersed in a Si grease are attached to the cantilevers so that the crystals are protected from moisture. As shown later, the observation of the quantum oscillations is direct evidence of high quality sample. The torque experiments were performed by a dilution refrigerator with a 20-T superconducting magnet and a He⁴ gas-flow cryostat with a 17-T superconducting magnet at Tsukuba Magnet Laboratories, NIMS.

Electronic band structure calculations are performed within the Perdew-Burke-Ernzerhof [17] generalized gradient approximation to DFT using the all-electron full-potential linearized augmented plane-wave method [18] as implemented in the HILAPW package [19]. the scalar relativistic scheme with spin-orbit coupling (SOC) as the second variation is employed during the self-consistent-field (SCF) calculations. Muffin-tin sphere radii of 0.9 Å for Na and 1.0 Å for Al and Si are adopted. Cutoff energies for the wave function and electron density are assumed to be 20 and 160 Ry, respectively. Uniform k -point meshes with $32 \times 32 \times 16$ are used for SCF loops and post density of states (DOS) and Fermi surface computations, respectively. The Fermi surface is drawn with the FermiSurfer application [20]. Experimental tetragonal crystal structures ($P4/nmm$) with lattice constants ($a = 4.1217$ Å and $c = 7.3629$ Å) and internal coordinates [$z(\text{Na}) = 0.63461$ and $z(\text{Si}) = 0.20764$] [6] are used throughout the present study. Our theoretical structure optimization leads to consistent structure data as

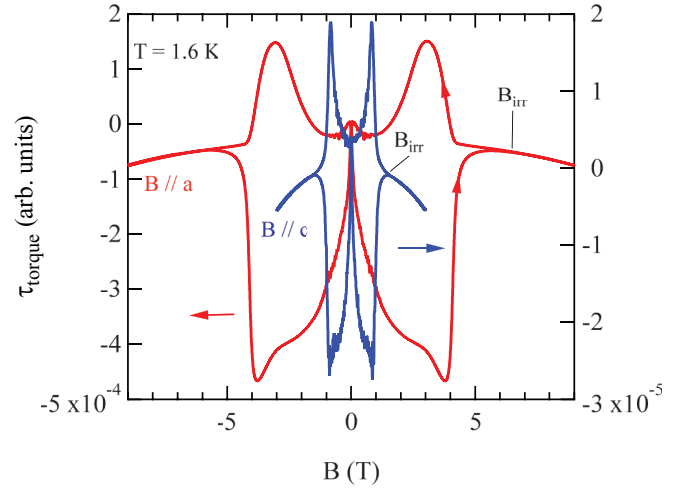


FIG. 2. Magnetic torque curves for $B // a$ and $B // c$ at 1.6 K. The hysteresis in a low field region is due to flux pinning in the superconducting state. The thick arrows indicate the irreversibility fields B_{irr} .

$a = 4.1395$ Å, $c = 7.3876$ Å, $z(\text{Na}) = 0.6358$, and $z(\text{Si}) = 0.2077$. Double-group irreducible representations and their time-reversal pairing or doubling for the obtained fully relativistic eigenstates are extracted by using the space-group analysis tools in the HILAPW package.

III. RESULTS

The magnetic torque is given by $\tau_{\text{torque}} = \mathbf{M} \times \mathbf{B}$, where \mathbf{M} and \mathbf{B} are the magnetization and magnetic field, respectively. Typical torque curves in fields parallel to the c and a axes are shown in Fig. 2. In a low field region, we see large torque signals due to the superconducting diamagnetism. The hysteretic behavior is ascribed to the pinning of the flux lines in the crystal. The up and down sweep signals coincide above 1.5 T for $B // c$ and 6.5 T for $B // a$, which are defined as the irreversibility fields B_{irr} . The flux lines move freely above B_{irr} , where the superconducting order parameter is significantly reduced. As expected from the definition, the irreversibility fields B_{irr} are slightly smaller than $B_{c2} = 1.6$ and 6.7 T determined from the resistance measurements, respectively [6]. At high fields in the normal phase, we observe quadratic behavior $\tau_{\text{torque}} \propto B^2$, due to the Pauli paramagnetism of the electronic states, $M \propto B$.

The QO measurement is a powerful tool to extract the Fermi surface structure and the relativistic nature of the Dirac fermions, Berry phase. The QO in the magnetization, M_{osc} is expressed by Lifshitz-Kosevich formula [21]. The QO in the torque, $\tau_{\text{osc}} \propto -[\partial F_i(\theta)/\partial \theta]M_{\text{osc}}$ is written as

$$\tau_{\text{osc}} \propto \left(\frac{\partial F_i}{\partial \theta} \right) B^{3/2} R_T R_D R_S \sin \left[2\pi \left(\frac{F_i(\theta)}{B} - \frac{1}{2} \right) + \varphi_0 + \varphi_B \right], \quad (1)$$

where R_T , R_D , and R_S are the temperature, Dingle, and spin-splitting reduction factors, respectively,

$R_T = (\kappa \mu_c T / B) / \sinh(\kappa \mu_c T / B)$, $R_D = \exp(-\kappa \mu_c T_D / B)$, and $R_S = \sin(\pi g^* \mu_c / 2)$. $\mu_c = m_c / m_0$ is the effective mass

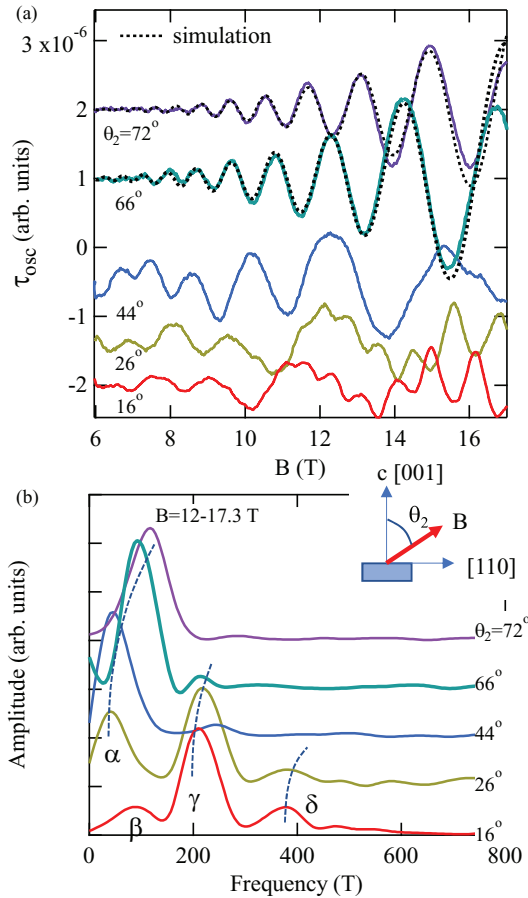


FIG. 3. (a) Oscillatory components of torque signals at various field angles for $T = 30$ mK. Dotted curves show simulated results by Eq. (1), giving $\varphi_B = 0.75\pi$ at $\theta_2 = 72^\circ$ and $\varphi_B = 0.8\pi$ at $\theta_2 = 66^\circ$. (b) Fourier spectra of the QOs in the range 12–17.3 T. The Fourier spectra are interpolated and then numerically smoothed. Four different peaks are evident, denoted as α , β , γ , and δ . The error of the frequency is roughly estimated as ± 20 T.

ratio (m_c : effective mass; m_0 : free electron mass), T_D is the Dingle temperature, g^* is the effective g factor, and κ is a constant value 14.7 K/T. In the oscillatory term, $F_i(\theta)$ is the QO frequency of the i th branch at the field angle θ , proportional to the extremal cross sectional area (A_{Fi}) of the Fermi surface, $F_i = (\hbar/2\pi e)A_{Fi}$. The phase φ_0 is $\pi/4(-\pi/4)$ for the extremal minimum (maximum) cross section of the Fermi surface. φ_B is the Berry phase on the cyclotron orbit.

Figure 3(a) presents oscillatory components of the torque curves at high fields, which are obtained by subtracting backgrounds fitted by polynomial functions. Here we define the field angles θ_1 from [001] to [100] and θ_2 from [001] to [110] as indicated in the insets of Figs. 3 and 4. At $\theta_2 = 16^\circ$ – 44° , we see low-frequency oscillations in the whole field region and high-frequency oscillations superimposed at high fields. Only single-frequency oscillations are seen at higher angles. In the Fourier transform (FT) spectra [Fig. 3(b)], three peaks denoted as β , γ , and δ are found at $\theta_2 = 16^\circ$, and then another branch α becomes evident at higher angles. The angular dependence of the frequencies in the two rotational planes are presented in Fig. 4. For $\theta_2 > 20^\circ$ and $\theta_1 > 30^\circ$, the frequency

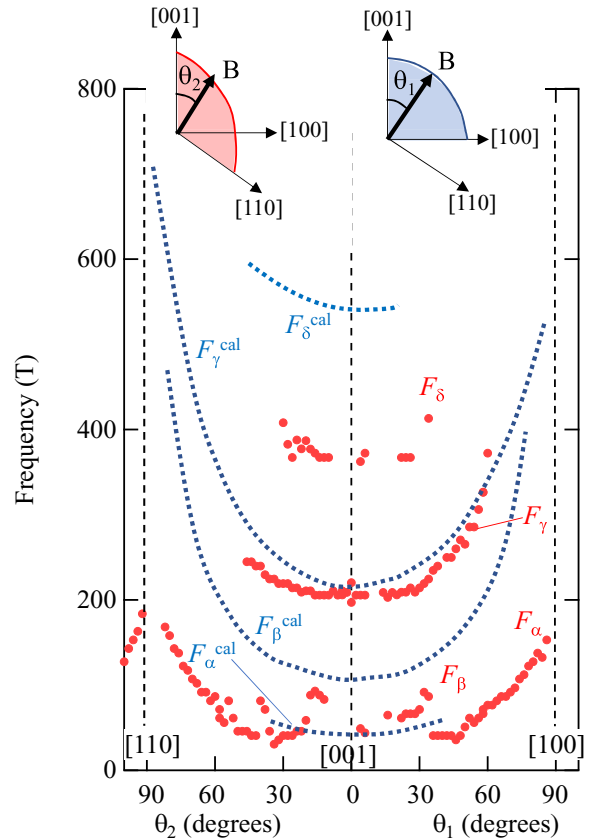


FIG. 4. Angular dependence of the QO frequencies in two different rotational planes. Dotted curves indicate the results by first-principle band calculations.

of α , F_α rapidly increases as the field is tilted toward [110] or [100]. The behavior suggests that α arises from an elongated Fermi surface along the k_z direction. Similar behavior is evident for F_γ . Only around $\theta_2 \approx 15^\circ$ and $\theta_1 \approx 30^\circ$, $F_\beta \approx 100$ T is observed. The largest frequency F_δ is observed in a limited angle region $\theta_1, \theta_2 < 30^\circ$. We obtain the frequencies for $B \parallel c$, $F_\alpha \approx 36$ T, $F_\beta \approx 65$ T, $F_\gamma \approx 206$ T, and $F_\delta \approx 360$ T. These values correspond to only 0.27%, 0.49%, 1.6%, and 2.7% of the Brillouin zone, respectively. Figure 5 presents the mass plots for α and γ , the FT amplitude divided by temperature as a function of temperature. The solid curves fitted with the function $\sinh(\kappa\mu_c T/B)$ show that the effective masses for α and γ are $0.75m_0$ and $1.1m_0$, respectively. The reliable masses for β and δ are not obtained because of the small oscillation amplitudes.

Figure 6(a) shows the calculated relativistic electronic band structure of NaAlSi around E_F , which is almost consistent with previous results [7–9, 15]. Each band as a function of the wave vector k is connected according to the double-group irreducible representation of the k group. One two-dimensional (2D) representation exists on the k lines of Δ , Σ , U , and S , where all the bands should be anticrossing. There are two 2D representations Λ_1 and Λ_2 on Λ . In particular, Λ_1 and Λ_2 bands close to E_F , are slightly split by SOC, being intimately related to the formation of complicated Fermi surfaces appearing around Z . Note that the Λ_1 and Λ_2 bands are completely degenerate by symmetry without SOC. On the Y and T lines,

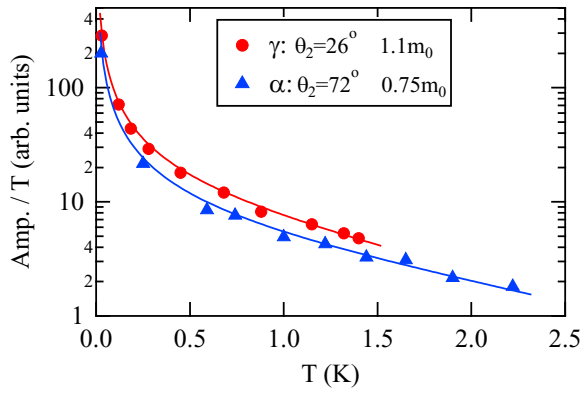


FIG. 5. Oscillation amplitude divided by temperature as a function of temperature. Solid curves indicate the fitted results by $\sinh(\kappa\mu_c T/B)$, giving the effective mass ratio, $\mu_c = 0.75m_0$ for α and $\mu_c = 1.1m_0$ for γ .

two pairs of four 1D representations are degenerate due to the time-reversal symmetry on the basis of Herring's criterion [22], resulting in two kinds of 2D bands; those are further degenerate without SOC. The size of the SOC splitting seen in bands on Y and T near the Fermi energy E_F seems to be smaller than that of the Λ_1 and Λ_2 bands mentioned above. This can be understood by the facts that the Λ_1 and Λ_2 bands are dominated by the Si p orbitals while the bands on the Y and T lines near the Fermi energy are largely hybridized with the s orbitals of Si and Al without SOC splitting. Flat bands

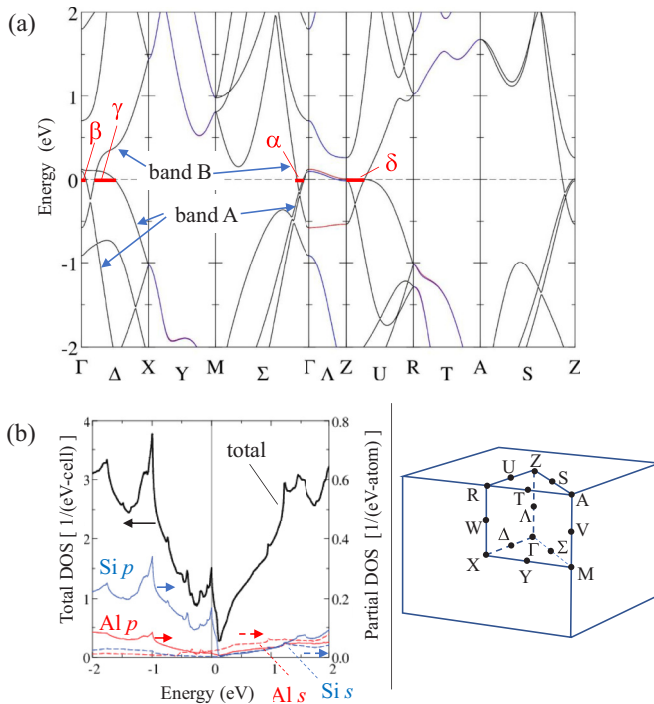


FIG. 6. (a) Calculated band structure of NaAlSi. The k regions corresponding to α , β , γ , and δ are indicated by red bars. (b) Total and partial density of states (DOS). Thick solid curve denotes total DOS while thin broken and solid (red and blue) curves display partial DOS projected on s and p orbitals, respectively.

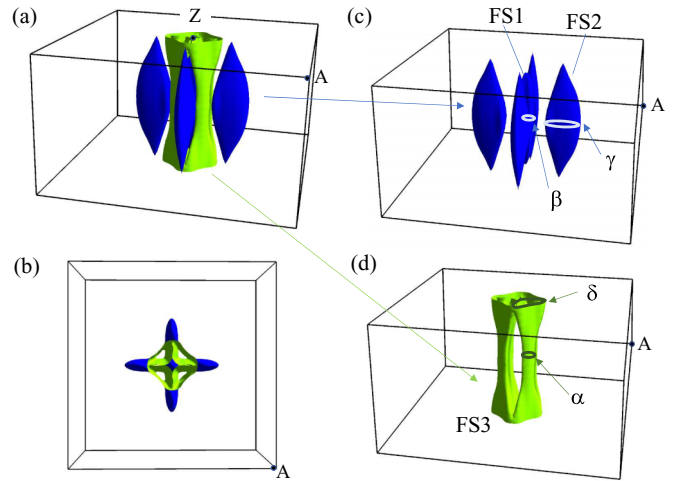


FIG. 7. Calculated Fermi surfaces of NaAlSi. Blue- and green-colored surfaces are made from bands A and B, respectively. Closed orbits corresponding to α , β , γ , and δ branches for $B \parallel c$ are indicated.

with saddle-point character around Z create very sharp peaks in DOS near the Fermi energy, as depicted in Fig. 6(b).

Two bands cross E_F , forming nearly 2D shaped Fermi surfaces as shown in Fig. 7. The band A in Fig. 6(a) makes a rounded square pillar Fermi surface around Γ (FS1). Four shell shaped surfaces are formed around Δ (FS2). Both of them are hole surfaces, closed just below and above the $k_z = \pm\pi/c$ planes. In addition, four radial-bone shaped electron surfaces are formed around Σ connecting at the $k_z = \pm\pi/c$ planes (FS3). The FS2 and FS3 are made of the two bands A and B.

In the Fermi surface structure, we note four extremal cross sections for $B \parallel c$ axis; β (maximum) of FS1, γ (maximum) of FS2, α (minimum), and δ (maximum) of FS3. Because of the elongated shape in the k_z direction, it is expected that all the cross sections increase as the field is tilted from [001] to [011] or [001]. The calculated frequencies corresponding to these cross sections, F_α^{cal} , F_β^{cal} , F_γ^{cal} , and F_δ^{cal} are indicated in Fig. 4 by dotted curves. The k -space range corresponding to each branch is indicated in Fig. 6(a). F_β^{cal} and F_γ^{cal} are well defined and smoothly increase with increasing ϕ or θ in wide angle ranges. In contrast to FS1 and FS2, FS3 is corrugated more finely, which makes it difficult to calculate the cross sections precisely. Among these four branches, F_δ^{cal} is very sensitive to the carrier number because the closed orbit arises from the flat band around Z . We should note that NaAlSi is unstable in the atmosphere, suggesting that a deviation from the stoichiometry changes the cross sections significantly.

The frequencies and masses are summarized in Table I. The effective mass m_c determined by QOs is generally given by $m_c = (1 + \lambda)m_b$, where λ and m_b are the mass enhancement factor due to many body effects and band mass obtained from the band calculations, respectively. We have the large factors, $\lambda = 2.0$ for α and 3.1 for γ . The mass enhancement will be responsible for the rather high $T_c \approx 7$ K in spite of the very small Fermi surfaces in NaAlSi.

TABLE I. Frequencies and masses for four branches.

Branch	F (T) expt./calc.	mass(m_0) $m_c(\text{expt.})/m_b(\text{calc.})$
$\alpha(\theta_2 = 72^\circ)$	117/-	0.75/25
$\beta(\theta_2 = 12^\circ)$	83/118	-/0.08
$\gamma(\theta_2 = 26^\circ)$	214/240	1.1/0.27
$\delta(\theta_2 = 10^\circ)$	367/540	-/1.59

IV. DISCUSSION

The topological nature of the electronic state can be directly evidenced by the nontrivial Berry phase φ_B which the electrons obtain on the cyclotron orbits in magnetic field. So far, the Berry phases have been determined by the QO measurements in various topological materials. The energy bands of NaAlSi have nodal lines in the k_z direction protected by the symmetries, which are interconnected with other nodal lines in the k_z planes [15]. In such complicated band structures, the nontrivial φ_B is not simply given [23], depending on the closed orbits: φ_B is sensitive to the magnetic field direction. In general, Landau fan diagrams produce rather large errors in the determination of φ_B when the wave shape is deformed by other frequencies or higher harmonic contents. In addition, a general scheme for describing φ_B in band dispersions including parabolic nature in addition to a Dirac cone shows that special attention should be paid in the Landau fan analyses [24]. The simulations by Eq. (1) will provide more reliable φ_B .

The α branch arises from the cyclotron orbit in the electron band near the Γ point as indicated in Fig. 6(a). We see a band crossing right below E_F , leading to a nontrivial φ_B . The QOs of the α branch for $\theta_2 = 66^\circ$ and 72° in Fig. 3(a) are simulated by Eq. (1), as presented by dotted curves. From the band characters, the wide s and p bands, we expect a small SOC, suggesting $g \approx 2$. From the relation $g^* \mu_c = gm_b/m_0$ [21], the spin-splitting reduction factor of the α branch will be

positive, $R_S > 0$. At $\theta_2 = 72^\circ$, we obtain $F_\alpha = 108$ T, $T_D = 3$ K, $\mu_c = 0.75$, and $\varphi_B = 0.75\pi$. Similarly, we have $F_\alpha = 89$ T, $T_D = 3.5$ K, $\mu_c = 0.56$, and $\varphi_B = 0.8\pi$ at $\theta_2 = 66^\circ$. For both cases, we obtain the nontrivial φ_B close to π . The result shows the small gap at the Dirac point due to the SOC and almost linear band dispersion at E_F for the α branch. For the other branches, we cannot obtain reliable φ_B because of too many fitting parameters.

An Fe based superconductor, FeSe has $T_c = 9$ K and small cylindrical Fermi surfaces with the QOs of $F = 100$ -700 T [25], similarly to NaAlSi. Since the superconducting energy gap $\Delta \approx 3$ meV is comparable to the Fermi energy $E_F = 3$ -10 meV [26], a crossover from a BCS to Bose-Einstein condensation (BEC) scheme has been discussed. For NaAlSi, we obtain $E_F \approx 200$ meV from the relation $E_F = \hbar^2 k_F^2 / 2m_c$ and $A_F = \pi k_F^2 = 2\pi eF/\hbar = 200$ nm $^{-2}$ for $F = 200$ T, or $E_F = 100$ -300 meV from the band calculations. The energy gap from the heat capacity measurements $\Delta \approx 2$ meV, which is much smaller than E_F , shows that the superconductivity in NaAlSi is far from the BCS-BEC crossover region.

V. CONCLUSION

The Fermi surface structures of the nodal-line semimetal NaAlSi are determined by magnetic QO measurements and the first-principles band calculations. The Fermi surfaces are composed of two small parts, electron- and holelike ones. The rather heavy effective mass of the Fermi surface around Γ shows the mass enhancement by many body effects, likely related to the superconducting mechanism. The nontrivial Berry phase is obtained for the α branch, consistent with the linear dispersion of the energy bands.

ACKNOWLEDGMENTS

The authors thank Dr. A. Tanaka for valuable discussions. This work was partly supported by Japan Society for the Promotion of Science (JSPS) KAKENHI Grants No. 20H05150 and No. 20H02820.

-
- [1] S.-Y. Guan, P.-J. Chen, M.-W. Chu, R. Sankar, F. Chou, H.-T. Jeng, C.-S. Chang, and T.-M. Chuang, Superconducting topological surface states in the noncentrosymmetric bulk superconductor PbTaSe $_2$, *Sci. Adv.* **2**, 600894 (2016).
- [2] L. He, Y. Jia, S. Zhang, X. Hong, C. Jin, and S. Li, Pressure-induced superconductivity in the three-dimensional topological Dirac semimetal Cd $_3$ As $_2$, *npj Quantum Mater.* **1**, 16014 (2016).
- [3] D. Kang, Y. Zhou, W. Yi, C. Yang, J. Guo, Y. Shi, S. Zhang, Z. Wang, C. Zhang, S. Jiang, A. Li, K. Yang, Q. Wu, G. Zhang, L. Sun, and Z. Zhao, Superconductivity emerging from a suppressed large magnetoresistant state in tungsten ditelluride, *Nat. Commun.* **6**, 7804 (2015).
- [4] X.-C. Pan, X. Chen, H. Liu, Y. Feng, Z. Wei, Y. Zhou, Z. Chi, L. Pi, F. Yen, F. Song, X. Wan, Z. Yang, B. Wang, G. Wang, and Y. Zhang, Pressure-driven dome-shaped superconductivity and electronic structural evolution in tungsten ditelluride, *Nat. Commun.* **6**, 7805 (2015).
- [5] W. Westerhaus and H.-U. Schuster, Darstellung und Struktur von NaAlSi und NaAlGe / preparation and structure of NaAlSi and NaAlGe, *Z. Naturforsch. B* **34**, 352 (1979).
- [6] T. Yamada, D. Hirai, H. Yamane, and Z. Hiroi, Superconductivity in the topological nodal-line semimetal NaAlSi, *J. Phys. Soc. Jpn.* **90**, 034710 (2021).
- [7] H. B. Rhee, S. Banerjee, E. R. Ylvisaker, and W. E. Pickett, NaAlSi: Self-doped semimetallic superconductor with free electrons and covalent holes, *Phys. Rev. B* **81**, 245114 (2010).
- [8] L. Jin, X. Zhang, T. He, W. Meng, X. Dai, and G. Liu, Topological nodal line state in superconducting NaAlSi compound, *J. Mater. Chem. C* **7**, 10694 (2019).
- [9] X. Yi, W. Q. Li, Z. H. Li, P. Zhou, Z. S. Ma, and L. Z. Sun, Topological dual double node-line semimetals NaAlSi(Ge) and their potential as cathode material for sodium ion batteries, *J. Mater. Chem. C* **7**, 15375 (2019).
- [10] S. Kuroiwa, H. Kawashima, H. Kinoshita, H. Okabe, and J. Akimitsu, Superconductivity in ternary silicide NaAlSi with layered diamond-like structure, *Phys. C (Amsterdam, Neth.)* **466**, 11 (2007).

- [11] M. J. Pitcher, D. R. Parker, P. Adamson, S. J. C. Herkelrath, A. T. Boothroyd, R. M. Ibberson, M. Brunelli, and S. J. Clarke, Structure and superconductivity of LiFeAs, *Chem. Commun.* (2008) 5918.
- [12] J. H. Tapp, Z. Tang, B. Lv, K. Sasmal, B. Lorenz, P. C. W. Chu, and A. M. Guloy, LiFeAs: An intrinsic FeAs-based superconductor with $T_c = 18$ K, *Phys. Rev. B* **78**, 060505(R) (2008).
- [13] Z. Deng, X. C. Wang, Q. Q. Liu, S. J. Zhang, Y. X. Lv, J. L. Zhu, R. C. Yu, and C. Q. Jin, A new “111” type iron pnictide superconductor LiFeP, *Europhys. Lett.* **87**, 37004 (2009).
- [14] L. Schoop, L. MÜchler, J. Schmitt, V. Ksenofontov, S. Medvedev, J. Nuss, F. Casper, M. Jansen, R. J. Cava, and C. Felser, Effect of pressure on superconductivity in NaAlSi, *Phys. Rev. B* **86**, 174522 (2012).
- [15] L. Muechler, Z. Guguchia, J. C. Orain, J. Nuss, L. M. Schoop, R. Thomale, and F. O. von Rohr, Superconducting order parameter of the nodal-line semimetal NaAlSi, *APL Mater.* **7**, 121103 (2019).
- [16] C. Rossel, P. Bauer, D. Zech, J. Hofer, M. Willemin, and H. Keller, Active microlevers as miniature torque magnetometer, *J. Appl. Phys.* **79**, 8166 (1996).
- [17] J. P. Perdew, K. Burke, and M. Ernzerhof, Generalized Gradient Approximation Made Simple, *Phys. Rev. Lett.* **77**, 3865 (1996).
- [18] E. Wimmer, H. Krakauer, M. Weinert, and A. J. Freeman, Full-potential self-consistent linearized-augmented-plane-wave method for calculating the electronic structure of molecules and surfaces: O₂ molecule, *Phys. Rev. B* **24**, 864 (1981).
- [19] T. Oguchi, in *Interatomic Potential and Structural Stability*, edited by K. Terakura and H. Akai (Springer, Berlin, 1993), pp. 33–41.
- [20] M. Kawamura, FermiSurfer: Fermi-surface viewer providing multiple representation schemes, *Comput. Phys. Commun.* **239**, 197 (2019).
- [21] D. Shoenberg, *Magnetic Oscillations in Metals* (Cambridge University Press, Cambridge, UK, 1984).
- [22] C. Herring, Effect of time-reversal symmetry on energy bands of crystals, *Phys. Rev.* **52**, 361 (1937).
- [23] C. Li, C. M. Wang, B. Wan, X. Wan, H.-Z. Lu, and X. C. Xie, Rules for Phase Shifts of Quantum Oscillations in Topological Nodal-Line Semimetals, *Phys. Rev. Lett.* **120**, 146602 (2018).
- [24] A. A. Taskin and Y. Ando, Berry phase of nonideal Dirac fermions in topological insulators, *Phys. Rev. B* **84**, 035301 (2011).
- [25] T. Terashima, N. Kikugawa, A. Kiswandhi, E.-Sang. Choi, J. S. Brooks, S. Kasahara, T. Watashige, H. Ikeda, T. Shibauchi, Y. Matsuda, T. Wolf, A. E. Böhmer, F. Hardy, C. Meingast, H. Löhneysen, M. T. Suzuki, R. Arita, and S. Uji, Anomalous Fermi surface in FeSe seen by Shubnikovde Haas oscillation measurements, *Phys. Rev. B* **90**, 144517 (2014).
- [26] S. Kasahara, T. Watashige, T. Hanaguri, Y. Kohsaka, T. Yamashita, Y. Shimoyama, Y. Mizukami, R. Endo, H. Ikeda, K. Aoyama, T. Terashima, S. Uji, T. Wolf, H. von Löhneysen, T. Shibauchi, and Y. Matsuda, Field-induced superconducting phase of FeSe in the BCS-BEC cross-over, *Proc. Natl Acad. Sci. USA* **111**, 16309 (2014).